INORGANIC CHEMISTRY
FRONTIERS

RESEARCH ARTICLE

View Article Online
View Journal | View Issue

Cite this: *Inorg. Chem. Front.*, 2024, **11**, 6089

Piano-stool metal complexes as inhibitors of amyloid-β aggregation *in vitro* and *in vivo*†

Gloria Vigueras, [a] Raimon Sabate,[b,c] Leoní A. Barrios, [c,d] Ana B. Caballero,*[c,d] Samanta Hernández-García, [f] Pau Bayón,[g] Fernando Gandía-Herrero, *[f] José Ruiz *[a] and Patrick Gamez [c,d,e]

Alzheimer's disease (AD) is the most common form of dementia worldwide. There is currently no cure for this neurodegenerative disorder, and the available therapies only temporarily lessen some symptoms rather than stopping the disease's progression. One of the pathological hallmarks in AD brains is the formation of amyloid-β plaques. Transition-metal complexes have aroused great interest as potential chemical modulators of Aβ aggregation thanks to intrinsic features such as the metal oxidation state or the coordination geometry. Four related piano-stool complexes with different metal ions, namely Ru(II), Os(II), Ir(III) and Rh(III), were prepared and their inhibition properties of Aβ aggregation were investigated. It was found that all of them favour an alternative folding pathway, impeding the formation of mature fibres. Moreover, the metal centre seems to play a crucial role in their inhibiting activities. Ru(II) (**1**), Ir(III) (**3**) and Rh(III) (**4**) compounds were remarkable inhibitors of Aβ aggregation *in vitro*, most particularly **4**, and they appear to share the inhibitory mechanism. However Os(II) complex **2** acts differently on the Aβ aggregation process. *In vivo* studies using a *Caenorhabditis elegans* animal model of AD revealed the potential of complexes **2** and **4**, with **2** exhibiting better inhibition potential than **4**, thus illustrating the possible occurrence of additional variables to the aggregation process when moving from *in vitro* experiments to a living organism. To the best of our knowledge, **2** is the first osmium complex reported as an effective inhibitor of amyloid-β aggregation both *in vitro* and *in vivo*.

Received 11th June 2024,
Accepted 24th July 2024

DOI: 10.1039/d4qi01460j

rsc.li/frontiers-inorganic

Introduction

Alzheimer's disease (AD) is a progressive neurodegenerative cerebral disease giving rise to synaptic reduction and cognitive decline, eventually leading to death.[1] AD is characterized by the presence of extracellular plaques of amyloid-β (Aβ) peptide and intracellular neurofibrillary tangles of hyperphosphorylated tau protein in the brain of patients.[2]

Targeting Aβ overproduction, aggregation and toxicity represents an active area of AD research in chemistry.[3–7] The roles of these pathological events in AD progression,[8,9] including the involvement of biometals like zinc and copper,[10,11] have been investigated thoroughly,[5,12] and they are still considered to be potential therapeutic targets.[13] Several anti-aggregation agents,[14,15] metal chelators[16,17] and antioxidants[18,19] have been developed in the last three decades.[20] However, the track record of success in AD clinical trials so far has been very poor. For that reason, the use of *in vivo* models of the disease is important to evaluate the potential of novel therapeutic approaches.[21,22]

The use of metal complexes to tackle neurological issues induced by Aβ is a research topic of growing interest.[23–26] Both AD therapy and diagnosis (*e.g.*, imaging) with transition-metal

[a]*Departamento de Química Inorgánica, Universidad de Murcia, Biomedical Research Institute of Murcia (IMIB-Arrixaca), E-30100 Murcia, Spain. E-mail: jruiz@um.es*
[b]*Departament de Farmàcia, Tecnologia Farmacèutica i Fisicoquímica, Secció Fisicoquímica, Facultat de Farmàcia i Ciències de l'Alimentació, Joan XXIII 27-31 08020-Barcelona, Joan XXIII 27-31, E-08020 Barcelona, Spain*
[c]*Institute of Nanoscience and Nanotechnology (IN2UB), Universitat de Barcelona, 08028 Barcelona, Spain*
[d]*Departament de Química Inorgànica i Orgànica, Secció Química Inorgànica, Facultat de Química, Universitat de Barcelona, Martí i Franquès 1-11, E-08028 Barcelona, Spain. E-mail: ana.caballero@ub.edu*
[e]*Catalan Institution for Research and Advanced Studies (ICREA), Passeig Lluís Companys 23, 08010 Barcelona, Spain*
[f]*Departamento de Bioquímica y Biología Molecular A, Unidad Docente de Biología, Facultad de Veterinaria. Regional Campus of International Excellence "Campus Mare Nostrum". Universidad de Murcia, E-30100 Murcia, Spain. E-mail: fgandia@um.es*
[g]*Departament de Química, Facultat de Ciències, Universitat Autònoma de Barcelona, Campus Bellaterra, 08193 Cerdanyola del Vallès, Barcelona, Spain*

†Electronic supplementary information (ESI) available. CCDC 2359733. For ESI and crystallographic data in CIF or other electronic format see DOI: https://doi.org/10.1039/d4qi01460j

complexes are currently being investigated.[27] For instance, ^{64}Cu, ^{68}Ga and ^{89}Zr complexes have been developed for PET imaging.[28] Fluorescent probes based on Ru(II), Re(I), Ir(III) and Pt(II) have been reported for the detection of Aβ aggregates.[29] ^{99m}Tc and ^{111}In coordination compounds have been used for SPECT imaging,[28] and Gd-based contrast agents have been designed for MRI applications.[27,30] Various transition metals, including Co(III), Ni(II), V(V), Rh(III), Ir(III), Ru(II), Ru(III) and Pt(II) have been studied as potential anti-AD agents.[31,32] A number of metal complexes have also been reported for theranostic applications, for example, some Ru(II),[33,34] Ir(III)[35] and Gd(III)[36] coordination species.[6,27]

In the last years, Ru(II) complexes have gained interest in the field of Aβ aggregation after reports on the use of polypyridyl-type[37,38] or NAMI-A-like[39,40] compounds. Hence, Ru(II)[41,42] and Ru(III)[43–45] complexes are increasingly described in the literature. Comparatively, Ir(III)[46] and Rh(III)[47] complexes to modulate Aβ aggregation are much less reported.

Piano-stool metal complexes have been reported to exhibit interesting inhibitory activities against Aβ aggregation,[48] and some benzimidazole scaffolds have been described to have anti-AD properties.[49,50]

Herein, the quinoline benzimidazole-based ligand **L1** (Chart 1) was used for the preparation of four piano-stool complexes with four different transition metals and two distinct π-arene rings: [RuCl(η^6-*p*-cym)**L1**]PF_6 (**1**), [OsCl(η^6-*p*-cym)**L1**]PF_6 (**2**), [IrCl(η^5-Cp*)**L1**]PF_6 (**3**) and [RhCl(η^5-Cp*)**L1**]PF_6 (**4**) (with *p*-cym = *p*-cymene and Cp* = pentamethylcyclopentadienyl). The effect of these complexes on the aggregation of Aβ *in vitro* was subsequently investigated by using thioflavin T (ThT) fluorescence, dynamic light scattering (DLS), transmission electron microscopy (TEM) and ESI-MS. Subsequently, *in vivo* assays were performed with *Caenorhabditis elegans* mutant strains expressing human amyloid peptide either in their body muscle or in their neurons. To the best of our knowledge, the first Os (II) complex acting as an inhibitor of amyloid-β aggregation both *in vitro* and *in vivo* has been identified.

Results and discussion

Preparation and characterization of compounds 1–4

Complexes **1–4** were typically prepared by reaction of the corresponding [(π-arene)MCl_2]$_2$ dimer and **L1** [51] in methanol at room temperature, as depicted in Scheme 1 (see Experimental section for details). The dimer precursors [(η^6-*p*-cymene)$RuCl_2$]$_2$,[52] [(η^6-*p*-cymene)$OsCl_2$]$_2$,[53] [(η^5-C_5Me_5)$IrCl_2$]$_2$ [54] and [(η^5-C_5Me_5)$RhCl_2$]$_2$ [54] were prepared as reported in the literature. The complexes were obtained with yields ranging from 42 to 87%. The compounds were characterized by NMR, UV-Vis spectroscopy, ESI-MS and elemental analysis.

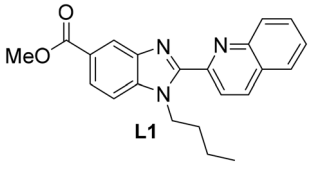

Chart 1 Methyl 1-butyl-2-(quinolin-2-yl)-1*H*-benzo[*d*]imidazole-5-carboxylate (**L1**).

The stability of the four complexes was evaluated in phosphate-buffered saline (PBS) containing 5% of DMSO ([complex] = 10 μM) for 24 hours at 37 °C, using UV-Vis spectroscopy (Fig. S1†). No spectral variations were observed for all compounds after one day, indicating that they remained unchanged in solution, under the conditions used. The decrease of the absorbance intensity observed for **4** suggests a gradual precipitation of the complex in PBS/5% DMSO.

Single crystals suitable for X-ray diffraction analysis were obtained from the slow diffusion of hexane into a saturated solution of complex **4** in CH_2Cl_2. This compound crystallizes in the triclinic space group $P\bar{1}$, and exhibits the typical "three-legged piano-stool" geometry with bond lengths ranging from 2.105(2) to 2.397(1) Å (Table S1†) and a π-ring centroid···Rh distance of 1.780(1) Å (Table S2†). A representation of the solid-state structure of **4** is given in Fig. 1. The coordination angles, including those involving the π-ring centroid, vary from 75.07(7) to 128.85(6)°. Bond lengths and angles are similar to those for other comparable organorhodium(III) complexes.[55,56] The full crystal data and structure refinement parameters are listed in Table S1,† and selected bond distances and angles are given in Table S2.†

In vitro evaluation of the anti-amyloid properties of 1–4 against Aβ40 peptide

The effect of complexes **1–4** on the aggregation of Aβ40 was investigated using thioflavin T (ThT), which gives strong fluorescence upon binding to amyloid fibrils characterized by the presence of β sheets (λ_{exc} = 450 nm; λ_{em} = 482 nm).[57] First, we verified that the fluorescence emission of **1–4** was falling out of that of ThT. Actually, all the compounds emit in the range 403–422 nm, which is far enough from the strong emission of amyloid-bound ThT at 482 nm (Fig. S2†).

The complexes were first incubated with monomeric Aβ40 at a 5-fold excess, and the protein aggregation was monitored in PBS at 37 °C (Fig. S3†). All the complexes completely inhibited Aβ40 aggregation as ThT fluorescence was not detected, even after 16 h (data not shown).

Given the efficacy shown by the four compounds at the tested complex-to-Aβ ratio of 5 : 1, aggregation experiments were then carried out at a lower molar ratio, namely 1 : 1 (Fig. 2). Under these conditions, distinct behaviours were observed for the different metal-containing compounds. To better compare their anti-amyloid behaviour, the aggregation curves were fitted to a two-step autocatalytic process (Scheme 2).[58] The calculated lag time (t_0), half aggregation time ($t_{1/2}$) and end time of the aggregation (t_1), are listed in Table 1. Ir(III) complex **3** and Rh(III) complex **4** drastically hinder amyloid aggregation, displaying nearly complete inhibition (Fig. 2). Thus, after 24 hours, 89 and 95% inhibition of Aβ40 aggregation were achieved respectively for **3** and **4**

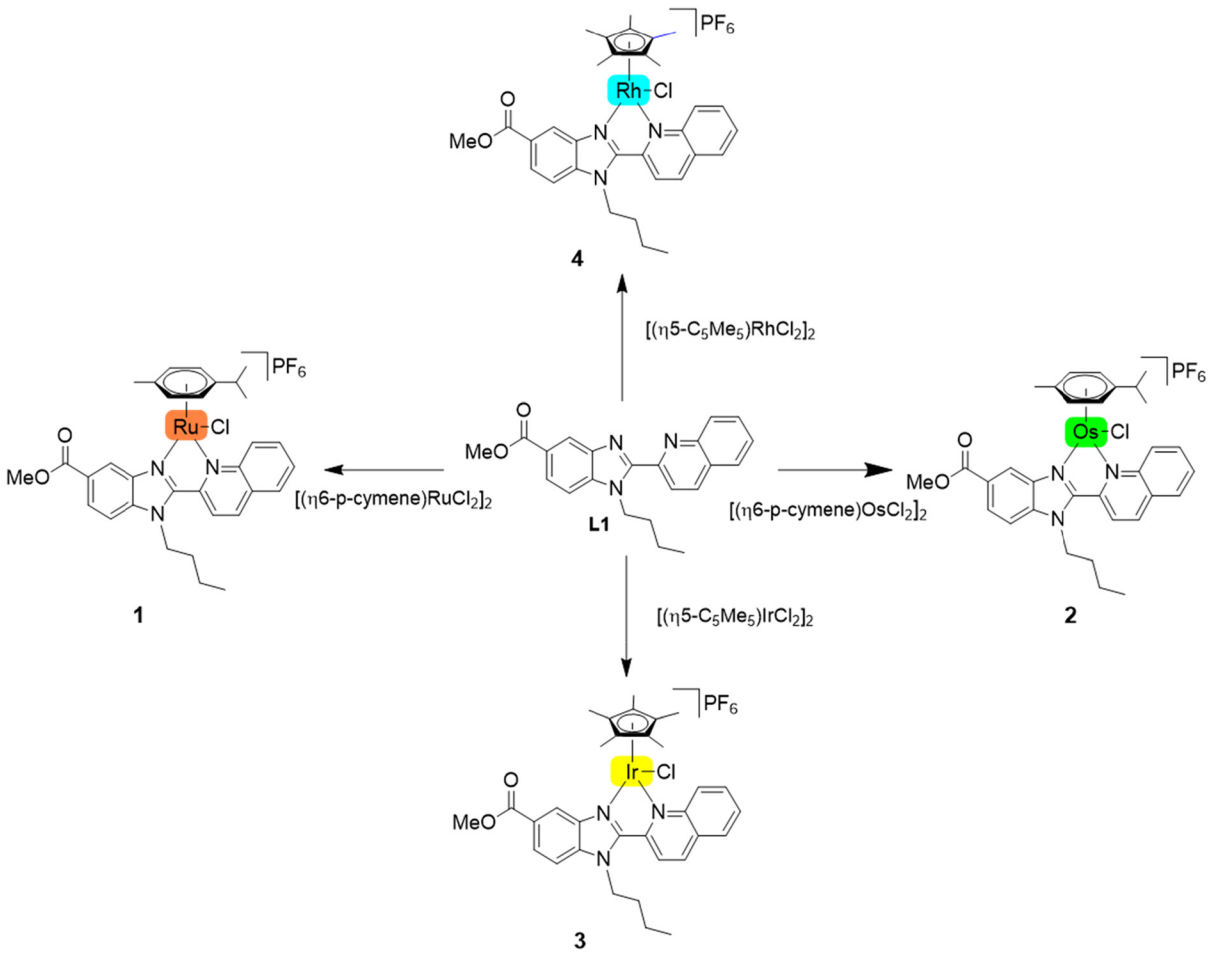

Scheme 1 Syntheses of complexes **1**–**4** from **L1**.

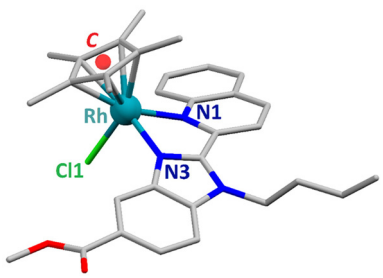

Fig. 1 Representation of the crystal structure of complex **4**. Hydrogen atoms, the PF_6^- counter ion and the lattice solvent molecule (*viz.* CH_2Cl_2) are omitted for clarity. The atoms involved in the coordination sphere are labelled, *C* standing for the centroid of the pentamethyl-cyclopentadienyl (Cp*) ring.

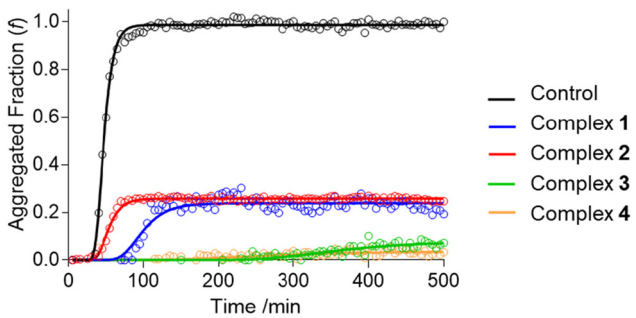

Fig. 2 Aggregation of Aβ40 in the presence of equimolar amounts of complexes **1**–**4**. [Aβ40] = 10 μM, PBS.

(Table 1). Ru(II) complex **1** and Os(II) complex **2** exhibited more modest inhibitory properties than **3** and **4**. Interestingly, while the inhibition by complex **1** shows an unequivocal increase in t_0, $t_{1/2}$ and t_1 (Table 1), these time values remain practically unaltered in the presence of **2**, suggesting different inhibition pathways. As shown in Fig. 2, complexes **3** and **4** increase the lag time (t_0) to 250–250 minutes (ThT fluorescence remains practically unchanged within these times), suggesting that these complexes might display a similar inhibitory mechanism to complex **1**.

Isostructural complexes **1** and **2** (with metals of group 8) led to analogous overall inhibition of amyloid aggregation but different pathways are suggested. Ru(II) compound **1** inhibits aggregation by delaying both the formation of nuclei and the subsequent fibrillation. In the case of isostructural **3** and **4**

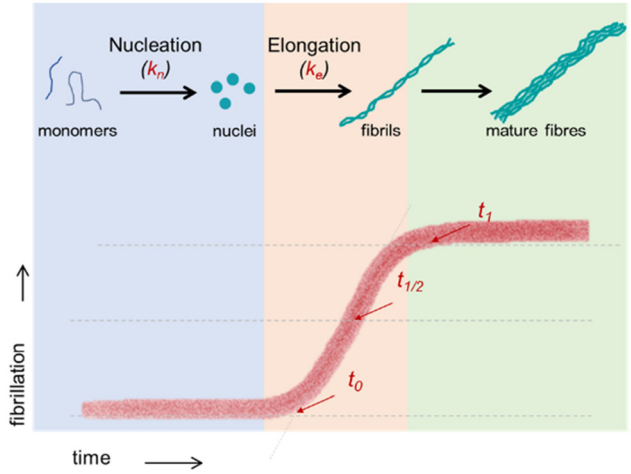

Scheme 2 Two-step (nucleation and elongation) autocatalytic fibrillation process of Aβ. t_0 = lag time before the formation of nuclei; $t_{1/2}$ = time required to aggregate half of the protein to its amyloid conformation; t_1 = time corresponding to the completion of the fibrillation process.

Table 1 Calculated kinetic parameters and experimental 24 h inhibition percentages for the aggregation of free Aβ40 and in the presence of equimolar amounts of complexes **1–4** [a]

	Control	1	2	3	4
t_0 (min)	34.1	53.4	39.0	—	—
$t_{1/2}$ (min)	47.4	98.4	53.7	—	—
t_1 (min)	60.8	143.4	68.4	—	—
Inhibition (%)	0.0	81.0	77.7	89.4	95.1

[a] [Aβ40] = 10 μM; [complex] = 10 μM. Standard error (SD) < 5%.

(with metals of group 9), hardly any differences in anti-aggregation activity were observed between them at equimolar concentrations to that of the protein. Unlike **1** and **2**, complexes **3** and **4** inhibited Aβ40 aggregation strongly, Rh(III) complex **4** being slightly stronger than Ir(III) compound **3**. Overall, neither the nature of the π-arene ligand nor the oxidation state of the metal ion seems to have a strong influence on the inhibitory properties of the complex; the variations noticed are clearly due to the nature of the metal ion.

At the end of each aggregation process (*i.e.*, after 24 h), the resulting suspensions of Aβ40 aggregates were analysed by dynamic light scattering (DLS, Fig. S5†) and transmission electron microscopy (TEM, Fig. 3). Complexes **3** and **4**, which exhibit analogous anti-aggregation properties, give rise to the generation of species with hydrodynamic diameter below 1.1 μm, which is the *Z*-average size of the aggregates formed by non-treated Aβ40. Very small species (in the 30–100 nm range) are also found in the presence of compound **4**. TEM images show these aggregates as short non-canonical fibrils and potential oligomeric species of protein, and their sizes agree with the hydrodynamic size measurements. These fibrils are ThT-silent because they lack amyloid mature structure. Compounds **1** and **2** led to comparatively bigger aggregates (over 1.1 μm) but their macroscopic morphology in TEM is rather different. Ribbon-like structures with appearance of long flexible fibrils are formed in the presence of **1**, while different fibril-like structures were found exclusively when the protein was treated with **2**. It should be noted that such fibrillated species formed with compound **2** were hardly found along the grid, which indicates qualitatively their lower amount. In concordance with the kinetic profiles, amyloid-like species shown by TEM in the presence of complexes **3** and **4** display similar macroscopic structures to those obtained in the presence of complex **1**, but they are shorter, particularly in the presence of complex **4**. This again suggests a shared inhibitory mechanism for complexes **1**, **3**, and **4**. Compiled data suggest that all compounds favour an alternative folding pathway, leading to aggregation in a non-canonical amyloid conformation hampering the formation of mature fibres.

To provide further insights on the mechanism of action of compounds **1–4**, samples of Aβ40 incubated with equimolar amounts of each compound for 24 h were analysed by ESI-MS (Fig. S7†). For compounds **1**, **3** and **4**, the MS spectra display a peak corresponding to the respective 1 : 1 protein adduct with (η^6-*p*-cymene)Ru, (η^5-C_5Me_5)Ir and (η^5-C_5Me_5)Rh. No metal-Aβ adducts were detected when the peptide was treated with **2**. These results suggest that the metal ions of compounds **1**, **3** and **4** bind the peptide upon losing both **L1** ligand and the labile chloride. Previously, Ma and coworkers had described the loss of a C^N-ligand in a Rh(III) complex to bind Aβ40, which resulted in a strong inhibition of the aggregation.[35] Strikingly, no evidence of such interaction was found for the Os(II) complex **2** in ESI-MS spectra. Hence, it is not clear how this compound acts beyond a suggested non-covalent binding.

For comparison, the four compounds were tested with the more aggregation-prone Aβ42 peptide, using the same concentration (10 μM) and conditions as with Aβ40. All of them, even compounds **1** and **2**, inhibited completely the amyloid aggregation in this case (Fig. S4†). Since Aβ42 is known to form a higher number of oligomers, the compounds might be more active because they act mainly in the nucleation phase. Further studies, which are out of the scope of this work, would be necessary to confirm this hypothesis.[59]

Since two alternatively mechanisms of inhibition have been suggested, we next investigated the effect of the concentration of complexes of the heaviest metals, *i.e.* **2** and **4**, which have shown very distinct behaviours. To compare their behaviour in more detail, the aggregation curves were fitted to a two-step autocatalytic process (Scheme 2).[58] Complex concentrations of 0.1, 1.0, 2.5 and 5 μM were used with a 10 μM solution of Aβ40. The resulting aggregation plots are shown in Fig. 4, and the calculated kinetic parameters, namely the nucleation rate constant (k_n), the elongation rate constant (k_e), the lag time (t_0), the half aggregation time ($t_{1/2}$) and the end time of the aggregation (t_1), are listed in Tables 2 and 3. As expected, a very different concentration-dependent behaviour was observed between both compounds.

The data suggest that compound **2** primarily accelerates the nucleation phase in a concentration-dependent manner

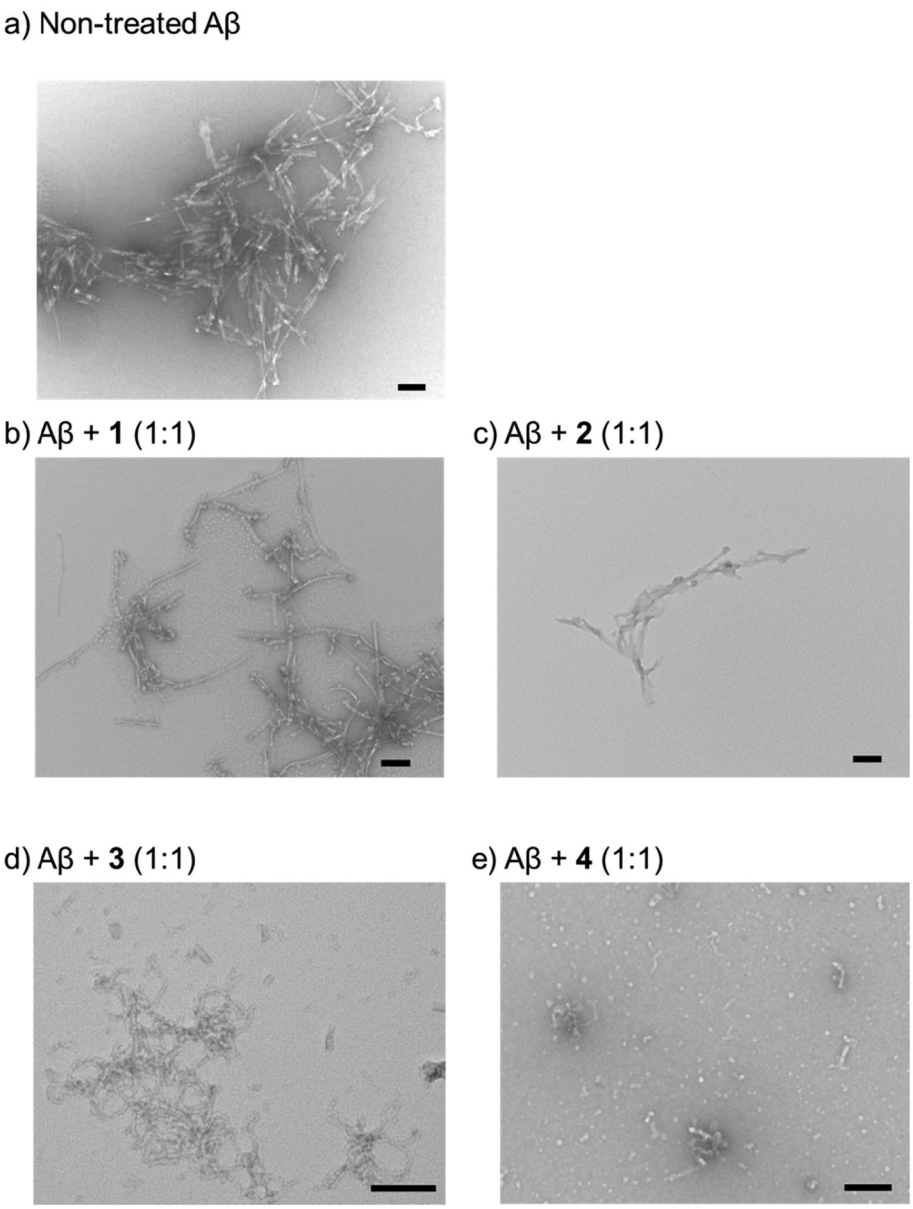

Fig. 3 TEM images of Aβ40 samples incubated for 24 h (a) without added compound, and with equimolar amounts of compounds **1**–**4** (b–e), respectively. [Aβ] = 10 μM; [complex] = 10 μM. Scale bar 100 nm.

(Table 2). At 5.0 μM, the nucleation constant increases four-fold. In contrast, the elongation constant is slightly reduced, indicating a slowdown in fibril elongation once the nuclei are formed. The accelerated nucleation may lead to the formation of non-canonical nuclei (*i.e.*, bad template nuclei) or amorphous species, impeding the formation of normal amyloid fibrils. In the presence of compound **2**, the final kinetic curves at all concentrations are comparable to those without the complex, as it occurred at equimolar concentrations (Fig. 2). Thus, because of the opposite effects on the nucleation constant (k_n) and the elongation constant (k_e), all the plots obtained appear to have the same shape as that observed for free Aβ40; only the plateaus -*i.e.* the final amount of fibres- are concentration-dependent and decrease with increasing concentration (Fig. 4a). We could hypothesize that the formation of non-canonical nuclei upon the interaction with the metal complex hinders the formation of normal amyloid fibrils, slowing down the fibril elongation.

The plots obtained for compound **4** (Fig. 4b) differ significantly from those for compound **2**. Complex **4** (which appear to share the behaviour of compounds **1** and **3**) reduces both nucleation and elongation processes, leading to an increase in all kinetic times (t_0, $t_{1/2}$, t_1) that is dependent on concentration (Table 3). In this case, the shape of the aggregation curve is strongly influenced by the concentration of compound **4**. Both the lag and elongation times are significantly altered as the

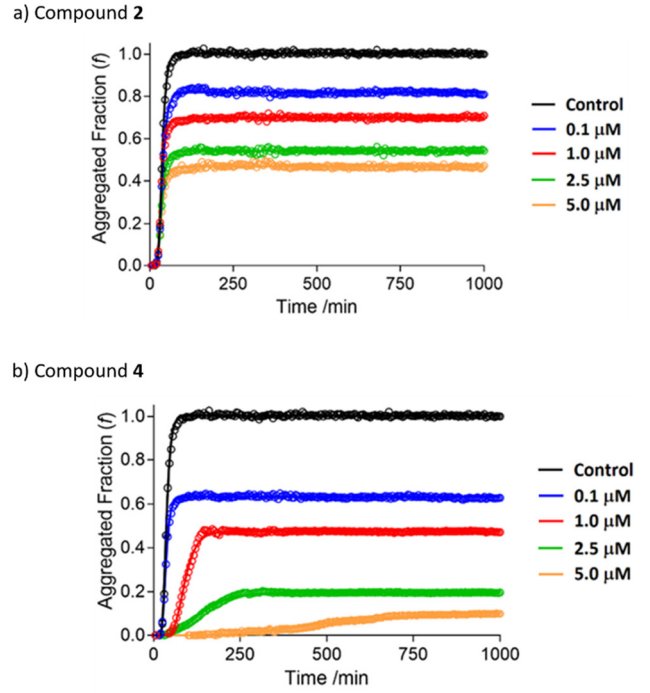

Fig. 4 Aggregation of Aβ40 (10 μM) in the presence of increasing concentrations of (a) complex **2** and (b) complex **4**.

Table 2 Kinetic parameters for the aggregation of free Aβ40 (10 μM) and in the presence of increasing amounts of complex **2**

	Control	0.1 μM	1.0 μM	2.5 μM	5.0 μM
k_n (10^{-6}·min^{-1})	271	505	482	495	992
k_e (M^{-1}·min^{-1})	17 390	15 210	16 530	16 160	13 940
t_0 (min)	23.9	23.3	22.8	23.0	21.3
$t_{1/2}$ (min)	36.8	36.9	34.4	34.9	34.5
t_1 (min)	49.6	50.5	46.0	46.7	47.6
Inhibition (%)	0.0	19.1	29.2	45.7	52.8

Standard error (SD) < 5%.

Table 3 Kinetic parameters for the aggregation of free Aβ40 (10 μM) and in the presence of increasing amounts of complex **4**

	Control	0.1 μM	1.0 μM	2.5 μM	5.0 μM
k_n (10^{-6}·min^{-1})	271	292	200	164	129
k_e (M^{-1}·min^{-1})	17 390	18 080	6317	2392	864
t_0 (min)	23.9	22.4	50.6	61.9	199.8
$t_{1/2}$ (min)	36.8	35.4	91.6	138.8	493.9
t_1 (min)	49.6	48.5	132.5	215.8	788.1
Inhibition (%)	0.0	37.2	52.9	80.4	90.2

Standard error (SD) < 5%.

complex-to-Aβ40 ratio increases. The formation of aggregates slows down as the concentration of compound **4** increases, and their final amount is significantly reduced; for example, nearly 80% inhibition of aggregation is achieved with 5 μM of **4** (Table 3). Thus, compound **4** acts as a very efficient kinetic inhibitor of aggregation, drastically reducing both nucleation and elongation processes. In summary, the data suggest that the coordination binding of this compound to Aβ40 occurs in the soluble species or during the initial nucleation events, resulting in the formation of non-productive nuclei and, consequently, impeding fibril elongation and the eventual formation of mature fibres. The effectiveness of the metal-to-protein binding is clearly demonstrated by the corresponding half-maximal inhibitory concentrations (IC_{50}), which are 4.50 μM and 0.36 μM for complex **2** and compound **4**, respectively—over 10 times lower for compound **4** (Fig. S6†).

Effects of the metal complexes *in vivo*

Given their distinct *in vitro* behaviour, complexes **2** and **4** were selected to carry out *in vivo* experiments with several *Caenorhabditis elegans* strains model of AD. Despite its simplicity, the human genome and the *C. elegans* genome share about 44% of the genes, including many genes and processes that cause human disorders. Therefore, such nematode can be used as an animal model for molecular mechanism research and *in vivo* drug testing. Moreover, gene editing has been simplified for this species to generate new phenotypes, including AD models.[60]

The CL4176 *C. elegans* strain contains a temperature-inducible transgene which produces human amyloid protein in the animal's muscle walls once the temperature is shifted from 16 °C to 25 °C.[61] Consequently, the worms suffer fast and irreversible paralysis due to the accumulation of Aβ aggregates in the body's walls. As a result, the nematodes are unable to move and feed, hence resulting in premature death. Treatment with **2** delayed the onset of paralysis by up to 7 hours (Fig. 5). Moreover, **2** led to an increase in the PT_{50} (Paralysis Time 50%) value (*viz.*, the mean time interval at which 50% of the worms were paralyzed), a key parameter to evaluate the nematode's motility.[62] The PT_{50} value for control animals was 45.6 ± 0.3 hours, whereas it increased up to 47.5 ± 0.3 hours with worms supplemented with complex **2**. Complex **4** did not increase the paralysis time in a significant manner (Fig. 5).

However, both complexes were able to significantly reduce the number of amyloid aggregates in the body wall muscle of the nematodes (Fig. 6). The CL2331 strain[63] contains a temperature-inducible transgene that produces human Aβ fused with GFP upon induction. Hence, the protein aggregates can easily be visualized under a microscope (Fig. 6a).[64] Complex **2** reduced by 30% (Fig. 6b and d) the formation of human Aβ aggregates in the animal's body, while **4** reduced the protein plaques by 25% (Fig. 6c and d). Moreover, complex **2** also protected neurons against Aβ-induced toxicity, as shown by the chemotaxis assays performed with the mutant strain CL2355 (Fig. 7). This strain expresses human Aβ in the nematode's neurons that give rise to an alteration of the chemotaxis behaviour induced by the protein toxicity.[65] The non-treated CL2322 nematodes, which were used as a control strain, had a chemotaxis index (C.I.) of 0.5 ± 0.1, while the CL2355 strain had a C.I. of 0.18 ± 0.07, showing how impaired the strain is due to amyloid accumulation in neurons. Treatment with complex **2**

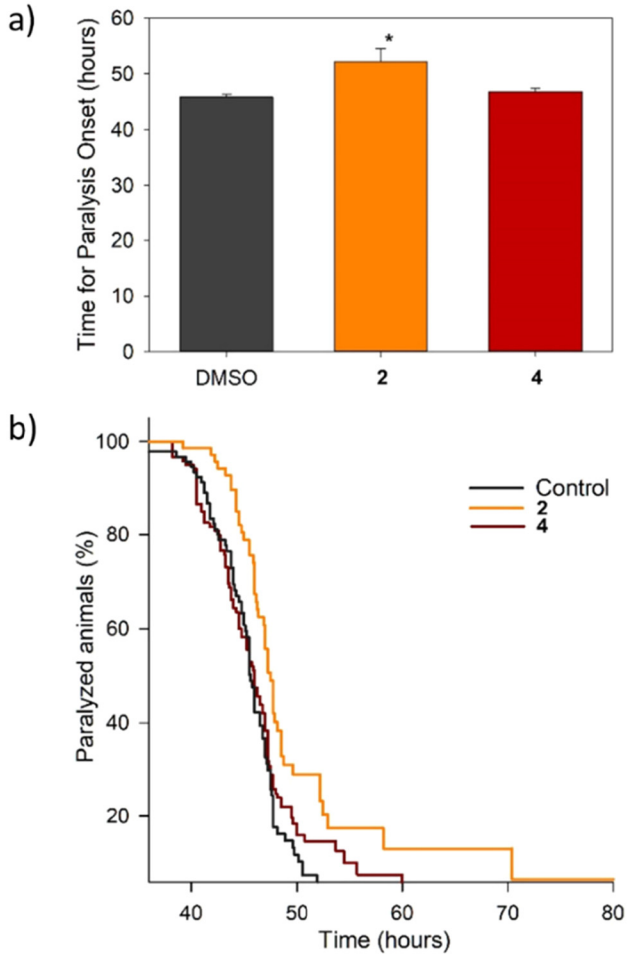

Fig. 5 Effect of metal complexes **2** and **4** (10 μM) on the strain CL4176 paralysis onset. (a) Paralysis time. (b) Paralysis curves. Data are represented as mean paralysis time ± standard error; three plates per condition were measured. * Significant at $p < 0.05$.

protected the neurons from Aβ toxicity, as illustrated by the C. I. of 0.52 ± 0.03 of the treated CL2355 animals.

The differences between the *in vitro* results, in which the amyloid protein is free, and those of a complete organism such as *C. elegans*, where the protein is expressed inside a tissue, could be due to the higher biological complexity of the nematodes and differences in the experimental conditions. Often, a combination of *in vitro* and *in vivo* studies is necessary to understand biological processes or the effects of a treatment fully. This is why we have used both approaches in this comprehensive study.

The discrepancy noted between *C. elegans* strains has been reported before. Gioran *et al.* reported that verbascoside reduced the paralysis of the animals, but no reduction in Aβ aggregate formation was shown.[66] The authors discussed that the apparent discrepancy could be due to the different strains used or that the mechanism of action did not necessarily involve only the reduction in Aβ aggregation. Nevertheless, in our study, complex **4** did not improve the PT50 but was able to prolong the paralysis time of the last nematodes, as shown in the paralysis curves (Fig. 5b). The maximum paralysis time, understood as the time in which the last worm was paralyzed, for complex **4** was 65.47 hours, while the maximum time for control nematodes was 60.34 hours. Thus, a tendency to improve the paralysis of the animals is shown for complex **4**, though complex **2** performed better in the biological assays for all the tested strains.

Experimental

Materials and methods

Common chemicals and solvents (HPLC grade or reagent grade quality) were purchased from commercial sources and used without further purification. Deuterated solvents were purchased from Euriso-top. ^{1}H and $^{13}C\{^{1}H\}$ NMR spectra were carried out on a Bruker AV 400 or Bruker AV 600 NMR spectrometer and chemical shifts are reported in ppm and cited relative to $SiMe_4$ and using the residual proton impurities in the solvents for ^{1}H and $^{13}C\{^{1}H\}$ NMR spectroscopy. Peak multiplicities are abbreviated as: s = singlet, m = multiplet, d = doublet, t = triplet, dd = doublet of doublet.

The C, H, and N analyses were performed with a Carlo Erba model EA 1108 microanalyzer, with an EAGER 200 software. The combustion of the samples was carried out in the presence of V_2O_5 and MgO as additives. The duration of the analysis was 15 minutes.

Direct insertion probe-mass spectrometry (MS-DIP). Mass spectra were recorded on an Agilent Q-TOF 6550 hybrid spectrometer with JetStream electrospray + i-Funnel ionization source. Mass spectrometry data were acquired in the positive ionization mode. The isotopic distribution of the heaviest set of signals matched very closely that of the calculated ones for the formulation of the complex cation in every case.

ESI-MS spectra of Aβ-containing samples were recorded on a Bruker timsTOF Pro2 instrument, equipped with an HPLC Bruker pump for sample injection, and calibrated with ESI-L Low Concentration Tuning Mix (Agilent Technologies). The measuring conditions were: 10 μL of sample injected at 50 $\mu L \cdot min^{-1}$ at 3.5–5.0 kV capillary-counter voltage, 90–110 °C of desolvation temperature, and dry gas at 6 $L \cdot min^{-1}$. The liquid carrier was a mixture of water : methanol (90 : 10) to avoid interaction with conventional ammonia buffers. Samples were prepared in PBS.

The UV-Vis spectra were registered using a PerkinElmer Lambda 750 S spectrometer. Fluorescence spectra were registered at room temperature with a HORIBA Jobin–Yvon iHR320 spectrofluorometer. The instrument excitation and emission slits were both set at 5 nm.

Synthesis of complexes 1–4

$[RuCl(\eta^6\text{-}p\text{-cym})L1]PF_6$ (1). L1 (359.4 mg, 1.0 mmol) was dissolved in freshly distilled methanol (30 mL) in a dry round-bottomed flask under a nitrogen atmosphere. $[(\eta^6\text{-}p\text{-cymene})RuCl_2]_2$ (306.2 mg, 0.5 mmol) was added with constant stirring. The resulting reaction mixture was stirred at room temp-

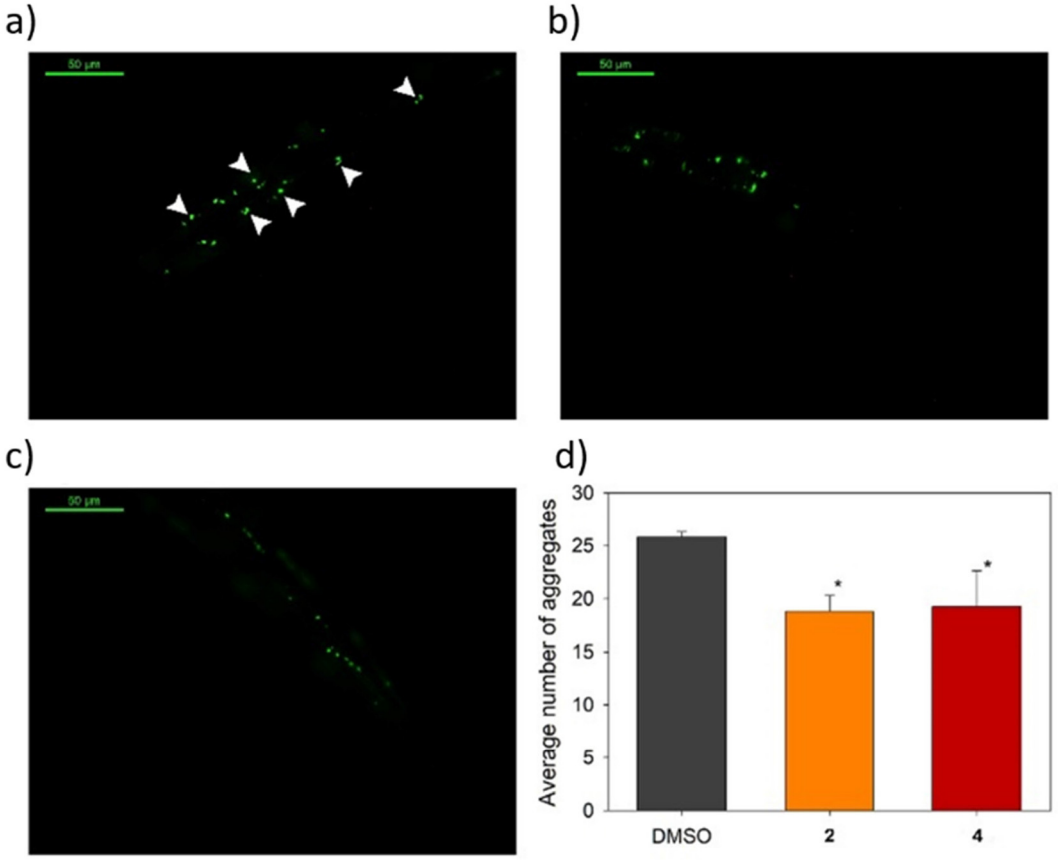

Fig. 6 Effect of metal complexes **2** and **4** ([complex] = 10 µM) on the aggregation of human amyloid protein *in vivo*. (a–c) Representative images of CL2331 worms treated with (a) DMSO (0.4%), (b) complex **2** and (c) complex **4**. (d) Results of the image analysis. Data are represented as mean values ± standard deviation. Two independent experiments were performed with $n > 15$. * Significant at $p < 0.05$ *vs*. DMSO control. Scale bar = 50 µm.

erature overnight. Then, the solution was concentrated to 15 mL and Bu_4NPF_6 in methanol (387.4 mg, 1.0 mmol) was added. The mixture was stirred for 30 minutes, producing a precipitate which was isolated by filtration, and washed with methanol and diethyl ether. The final product **1** was obtained with a yield of 52%. **^{1}H NMR (400 MHz, $CDCl_3$)** δ 8.99 (d, J = 8.5 Hz, 1H), 8.71 (d, J = 8.5 Hz, 1H), 8.64 (s, 1H), 8.40 (d, J = 8.7 Hz, 1H), 8.29 (dd, J = 8.7, 1.2 Hz, 1H), 8.09–8.01 (m, 2H), 7.88–7.83 (m, 1H), 7.72 (d, J = 8.7 Hz, 1H), 5.86–5.84 (m, 2H), 5.74–5.72 (m, 2H), 5.14–5.04 (m, 1H), 4.76–4.66 (m, 1H), 4.04 (s, 3H), 2.79–2.70 (m, 1H), 1.99 (s, 3H), 1.94–1.84 (m, 2H), 1.50–1.40 (m, 2H), 1.18–1.14 (m, 6H). 0.97 (t, J = 7.2 Hz, 3H) ppm (Fig. S8†). **^{13}C NMR (151 MHz, $CDCl_3$)** δ 167.1, 151.5, 150.8, 149.0, 142.4, 141.4, 140.4, 133.7, 131.0, 130.3, 130.1, 129.0, 128.8, 121.2, 120.8, 113.5, 108.9, 101.8, 86.8, 86.5, 85.8, 83.2, 53.7, 47.6, 32.8, 32.3, 24.1, 22.2, 21.1, 18.9, 14.6 ppm (Fig. S8†). ESI-MS (positive mode, CH_2Cl_2): m/z = 630.1474 ($[M - PF_6]$)$^+$ (Fig. S9†); anal. calcd for $C_{32}H_{35}ClF_6N_3O_2PRu$ (775.12): C, 49.58; H, 4.55; N, 5.42; found: C, 49.32; H, 4.21; N, 5.67 (%).

[OsCl(η^6-*p*-cym)L1]PF_6 (2). L1 (359.4 mg, 1.0 mmol) was dissolved in freshly distilled methanol (30 mL) in a dry round-bottomed flask under a nitrogen atmosphere. $[(\eta^6\text{-cymene})OsCl_2]_2$ (395.4 mg, 0.5 mmol) was added with constant stirring. The resulting reaction mixture was stirred at room temperature overnight. Then, the solution was concentrated to 15 mL and Bu_4NPF_6 in methanol (387.4 mg, 1.0 mmol) was added. The mixture was stirred for 30 minutes, producing a precipitate which was isolated by filtration, and washed with methanol and diethyl ether. The final product **2** was obtained with a yield of 87%. **^{1}H NMR (400 MHz, $CDCl_3$)** δ 8.82 (d, J = 8.7 Hz, 1H), 8.67 (d, J = 8.7 Hz, 1H), 8.54 (d, J = 1.1 Hz, 1H), 8.46 (d, J = 8.7 Hz, 1H), 8.32 (dd, J = 8.7, 1.4 Hz, 1H), 8.08 (dd, J = 8.1, 1.0 Hz, 1H), 7.99 (ddd, J = 8.7, 6.8, 1.4 Hz, 1H), 8.821 (ddd, J = 8.1, 6.8, 1.0 Hz, 1H), 7.74 (d, J = 8.7 Hz, 1H), 6.10–6.07 (m, 2H), 6.02 (d, J = 5.6 Hz, 1H), 5.96 (d, J = 5.6 Hz, 1H), 5.16–5.11 (m, 1H), 4.84–4.79 (m, 1H), 4.04 (s, 3H), 2.55–2.48 (m, 1H), 2.19 (s, 3H), 1.96–1.88 (m, 2H), 1.54–1.41 (m, 2H), 1.05 (d, J = 6.9 Hz, 3H), 0.99–0.94 (m, 6H) ppm (Fig. S10†). **^{13}C NMR (151 MHz, $CDCl_3$)** δ 167.0, 153.4, 151.0, 148.1, 142.6, 140.7, 139.9, 134.0, 131.23, 131.1, 130.3, 130.2, 129.3, 129.0, 120.8, 120.7, 113.7, 99.6, 95.9, 77.3, 77.0, 76.0, 75.6, 53.7, 47.4, 33.0, 32.2, 24.3, 22.3, 21.0, 19.1, 14.6 ppm (Fig. S10†). ESI-MS (positive mode, CH_2Cl_2): m/z = 720.1951 ($[M - PF_6]$)$^+$ (Fig. S11†); anal. calcd for $C_{32}H_{35}ClF_6N_3O_2OsP$ (865.16): C, 44.47; H, 4.08; N, 4.86; found: C, 44.76; H, 4.24; N, 4.76 (%).

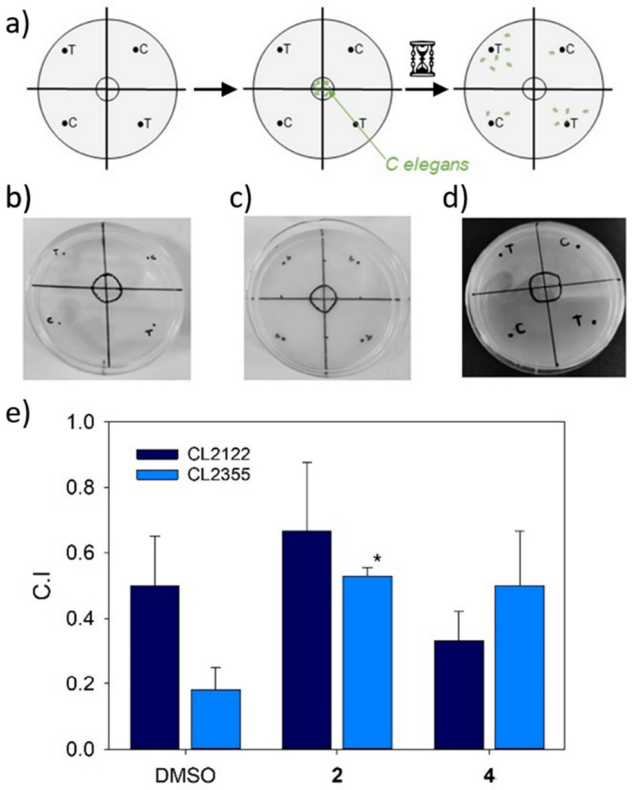

Fig. 7 Effect of **2** and **4** on the chemotactic behaviour of the *C. elegans* strains CL2122 and CL2355. (a) Chemotaxis assay scheme, C being the control quadrants and T the attractant quadrants. (b–d) Representative images of a clean chemotaxis plate (b), a plate once the worms were placed (c), and (d) a plate at the end of the experiment. (e) Calculated chemotaxis indexes. Data are represented as mean values ± standard deviation. Three C.I. plates were assayed for each condition; two independent trials were performed. *Significant at $p < 0.05$.

[IrCl(η^5-Cp*)L1]PF_6 (3). L1 (359.4 mg, 1.0 mmol) was dissolved in freshly distilled methanol (30 mL) in a dry round-bottomed flask under a nitrogen atmosphere. [(η^5-C_5Me_5)$IrCl_2$]$_2$ (398.4 mg, 0.5 mmol) was added with constant stirring. The resulting reaction mixture was stirred at room temperature overnight. Then, the solution was concentrated to 15 mL and Bu_4NPF_6 in methanol (387.4 mg, 1.0 mmol) was added. The mixture was stirred for 30 minutes producing a precipitate which was isolated by filtration, and washed with methanol and diethyl ether. The final product **3** was obtained with a yield of 67%. **^{1}H NMR (400 MHz, $CDCl_3$)** δ 8.69 (d, J = 8.5 Hz, 2H), 8.47–8.45 (m, 2H), 8.27 (dd, J = 8.8, 1.5 Hz, 1H), 8.06 (d, J = 8.2 Hz, 1H), 7.95–7.90 (m, 1H), 7.81 (t, J = 7.6 Hz, 1H), 7.71 (d, J = 8.8 Hz, 1H), 5.28–5.19 (m, 1H), 4.77–4.69 (m, 1H), 4.02 (s, 3H), 1.91–1.82 (m, 2H), 1.58 (s, 15H), 1.51–1.41 (m, 2H), 0.98 (t, J = 7.3 Hz, 3H) ppm (Fig. S12†); **^{13}C NMR (100.60 MHz, $CDCl_3$)** δ 166.8, 153.8, 148.5, 148.1, 142.7, 140.1, 138.0, 133.8, 131.1, 130.9, 130.4, 129.9, 128.8, 128.3, 121.2, 120.7, 113.7, 90.5(5C), 53.6, 47.3, 32.6, 21.0, 14.5, 10.2(5C) ppm (Fig. S12†). ESI-MS (positive mode, CH_2Cl_2): m/z = 722.2123([M − PF_6])$^+$ (Fig. S13†); anal. calcd for $C_{32}H_{36}ClF_6IrN_3O_2P$ (867.17): C, 44.32; H, 4.18; N, 4.85; found: C, 44.56; H, 4.32; N, 4.62 (%).

[RhCl(η^5-Cp*)L1]PF_6 (4). L1 (359.4 mg, 1.0 mmol) was dissolved in freshly distilled methanol (30 mL) in a dry round-bottomed flask under a nitrogen atmosphere. [(η^5-C_5Me_5)$RhCl_2$]$_2$ (309 mg, 0.5 mmol) was added at room temperature with constant stirring. Then, the solution was concentrated to 15 mL and Bu_4NPF_6 in methanol (1.0 mmol) was added in it. The mixture was stirred for 30 minutes producing a precipitate which was isolated by filtration, washed with methanol and diethyl ether. The final product **4** was obtained with a yield of 42%. **^{1}H NMR (400 MHz, $CDCl_3$)** δ 8.74 (dd, J = 14.1, 8.8 Hz, 2H), 8.52 (d, J = 0.7 Hz, 1H), 8.46 (d, J = 8.8 Hz, 1H), 8.24 (dd, J = 8.8, 1.5 Hz, 1H), 8.07 (d, J = 8.1 Hz, 1H), 7.98–7.94 (m, 1H), 7.84–7.78 (m, 1H), 7.69 (d, J = 8.8 Hz, 1H), 5.23–5.16 (m, 1H), 4.70–4.63 (m, 1H), 4.02 (s, 3H), 1.88–1.81 (m, 2H), 1.56 (s, 15H), 1.49–1.40 (m, 2H), 0.99 (t, J = 7.3 Hz, 3H) ppm (Fig. S14†); **^{13}C NMR (100.60 MHz, $CDCl_3$)** δ 167.0, 151.0, 148.7, 148.6, 142.5, 140.8, 138.8, 133.5, 130.9, 130.5, 130.3, 129.7, 128.5, 128.2, 121.6, 121.2, 113.5, 98.4, 98.3, 53.6, 47.5, 32.5, 21.1, 14.5, 10.4(5C) ppm (Fig. S14†). ESI-MS (positive mode, CH_2Cl_2): m/z = 632.1527 ([M − PF_6])$^+$ (Fig. S15†); anal. calcd for $C_{32}H_{36}ClF_6N_3O_2PRh$ (777.11): C, 49.40; H, 4.66; N, 5.40; found: C, 49.58; H, 4.87; N, 5.64 (%).

X-ray studies

Data for compound **4** was collected on a Bruker APEX II QUAZAR diffractometer equipped with a microfocus multilayer monochromator with Mo Kα radiation (λ = 0.71073 Å). Data reduction and absorption corrections were performed by using SAINT and SADABS, respectively.[67,68] The structure was solved using SHELXT and refined with full-matrix least squares on F^2 by using SHELXL.[69] Details can be found in CCDC 2359733† which contains the supplementary crystallographic data for this structure.

In vitro evaluation of the anti-amyloid properties

Preparation of Aβ monomer samples. Aβ(1-40) and Aβ(1-42), herein referred to as Aβ40 and Aβ42, respectively, were acquired from Bachem (Germany) as a trifluoroacetate salt. For the preparation of aggregate-free Aβ aliquots, a 5 mg-vial of Aβ was dissolved in 1,1,1,3,3,3-hexafluoro-2-propanol (HFIP, 1 mL) under vigorous shaking at room temperature for 1 h, after which it was sonicated for 30 min. The solution was further shaken for 1 h and cooled at 4 °C to minimise solvent evaporation during aliquotation. Aliquots of soluble Aβ were collected and left open to air overnight for HFIP evaporation. The resulting films of Aβ were stored at −20 °C. The amount of protein per sample was checked by spectrophotometry in 100 mM HEPES (pH 7.4) using the molar absorptivity $\varepsilon_{(Tyr,\ 280\ nm)}$ = 1490 M^{-1} cm^{-1}.

***In vitro* Aβ40 aggregation kinetics monitored by ThT fluorescence.** A FLUOstar Omega plate reader (BMG Labtech) in top optics configuration was used in fluorescence mode with ex440/em490 filters. The samples were measured in 96-well plates with black bottom. Aβ40 aliquots (see preparation

above) were dissolved in 30 μL of DMSO and sonicated for 15 min. In the plates, the samples were brought to 200 μL with PBS pH 7.4, giving final concentrations of 10 μM Aβ40, 14 μM ThT, and complex concentrations from 0 to 10 μM, unless stated otherwise. Stock solutions of 1 mM for ThT and metal complexes in DMSO were used. Kinetic measurements were initiated in the plate reader immediately after sample preparation. Endpoint measurements were performed at 37 °C every 5 min with continuous shaking (700 rpm, double-orbital mode).

Dynamic light scattering (DLS) assays. The hydrodynamic size distribution of protein aggregates was determined by dynamic light scattering with a Zetasizer Nano (Malvern, UK) at 25 °C. Solutions containing 10 μM of Aβ40 and 10 μM of compounds **1–4** in PBS were used and vortexed 30 s before measurements.

Transmission electron microscopy (TEM). Carbon-coated copper grids of 200 mesh were activated through glow discharge for 30 s. Immediately after that, the samples were deposited onto the grids, which were thoroughly washed with Milli-Q water. Then, the grids were treated with uranyl acetate 2% and left drying in a desiccator for at least 24 h before visualization. The samples were visualized at the Centres Científics i Tecnològics of the Universitat de Barcelona (CCiTUB), using a Tecnai Spirit TWIN (FEI) 120 kV TEM microscope equipped with a LaB_6 emitter and a Megaview 1k × 1k CCD.

Fitting of kinetic curves of *in vitro* Aβ40 aggregation. To determine the kinetic and thermodynamic parameters, the amyloid aggregation was approached mathematically as an autocatalytic reaction using eqn (1):

$$f = \frac{\rho\{\exp[(1+\rho)kt] - 1\}}{1 + \rho\exp[(1+\rho)kt]} \quad (1)$$

where f is the fraction of peptide in fibrillar form, the constant rate k includes the kinetic contributions of the nucleation (rate constant k_n) and elongation (rate constant k_e) processes of the fibrils, and ρ is a dimensionless parameter describing the relationship between k_n and k. eqn (1) was obtained under the boundary conditions of $t = 0$ and $f = 0$, where $k = k_e a$ (a being the peptide concentration). By non-linear regression of f against t, the values of ρ and k were obtained, and from them, the rate constants k_n and k_e. The extrapolation of the linear portion of the sigmoid curve to the abscissa ($f = 0$) and the highest ordinate value of the fitted plot affords 2 time values, corresponding to the lag time (t_0) and the end time (t_1); the time of half-aggregation ($t_{1/2}$) was considered to be the time when $f = 0.5$.[58,70] The analysis was performed using GraphPad Prism 10 for Win.

In vivo experiments

***C. elegans* strains and culture conditions.** The mutant strains CL4176 (*dvIs27 [myo-3p::A-Beta (1-42)::let-851 3′UTR) + rol-6(su1006)]*), CL2122 (*dvIs15 [(pPD30.38) unc-54(vector) + (pCL26) mtl-2::GFP]*), CL2355 (dvIs50 [pCL45 (snb-1::Abeta 1-42::3′ UTR(long) + mtl-2::GFP]) and CL2331 (dvIs37 [myo-3p::GFP::A-Beta (3-42) + rol-6(su1006)]) were kindly donated by the Caenorhabditis Genetic Centre (CGC, St Paul, MN, USA), which is funded by the NIH Office of Research Infrastructure Programs (P40 OD010440). All the strains were maintained at 16 °C in solid nematode growth medium (NGM). The *Escherichia coli* strain OP50 was used as a food source. *E. coli* was grown overnight in LB (Luria–Bertani) medium at 37 °C and was concentrated 10× in sterile M9 buffer.

All the worms used in the experiments were age-synchronized. The eggs were left at 16 °C to hatch over 24 hours. Once hatched, 25–30 **L1** larvae were transferred to 50 mm analysis plates (3–6 plates per condition), containing 8 mL of NGM agar, the metal complexes at 10 μM and 100 μL of *E. coli* OP50. The animals were maintained at 16 °C for 36 hours, and then the temperature was increased to 25 °C for transgene induction.

The phenotypes were verified with the visible gene marker *rol-6* for the strains CL2331 and CL4176 and the fluorescent constitutive *mtl-2:GFP* for the CL2355 and CL2122 strains.

Paralysis assay. The paralysis assay was monitored automatically using the Lifespan machine. CL4176 **L1** larvae were transferred into assay plates containing 8 mL of NGM agar, 10 μM of the metal complexes, and 100 μL of *E. coli* OP50. The prepared plates were placed in the Lifespan Machine scanners, the temperature was maintained at 16 °C for 36 hours and subsequently increased to 25 °C. The software was programmed to obtain an image of every plate at one-hour intervals. The experiment ended once all the worms in the plates were paralysed. All the plates' assays were done in triplicate, and four control plates were included in every assay. The Lifespan Machine was used following the constructor's instructions described by Stroustrup *et al.* with the modifications described by Guerrero-Rubio *et al.*[71,72]

Effect of the metal complexes on Aβ accumulation *in vivo*. The *C. elegans* strain CL2331 was used to study the potential of the metal complexes to reduce the formation of Aβ aggregates *in vivo*. Worms were maintained in assay plates containing the compounds, and after 36 hours at 16 °C the temperature was raised to 25 °C for 24 hours. Then the animals were washed with M9 buffer and mounted onto microscope glass slides containing 10 mM sodium azide to reduce their movement. Images were taken at 20× lens, using the GFP filter I3 in a fluorescence microscope Leica DM 2500 LED fitted with a Leica DFC550 camera (Leica Microsystems, Wetzlar, Germany). The number of Aβ fluorescent aggregates was counted with ImageJ software (NIH) 30. Briefly, each fluorescent image was split into red, blue, and green channels, blue and red channels were discarded, and the "Threshold" tool was applied only to the green channel. With the tool "Analyze Particles", the number of aggregates present in each animal was counted.[64]

***C. elegans* chemotaxis assay.** The strain CL2355 was used as a model of Aβ accumulation in neurons. This strain produces a worm phenotype that fails in chemosensory behavioral assays. Animals were maintained in plates supplemented with the compounds for 36 hours at 16 °C and 24 hours at 25 °C; then, the animals were washed three times in basal medium and placed in chemotaxis plates. CL2122 worms were used as a control strain.

The chemotaxis plates were prepared following the Margie, Palmer, and Chin-Sang's protocol.[73] Then, the worms were placed in the center of the plate in a drop of buffer, and the plates were left in the dark at 25 °C for one hour. This procedure was done in triplicate for both strains treated with the metal complexes and DMSO. Two independent experiments were performed.

After one hour at 25 °C, the animals in each quadrant were counted, and the chemotaxis index was calculated using the eqn (2) obtained from established protocols:

$$\text{C.I} = \frac{\text{total number of worms in } T - \text{total number of worms in } C}{n\,\text{total number of worms in } T + C} \quad (2)$$

Data statistical analysis. Mathematical analysis of the data obtained in the Lifespan Machine was performed using the Sigmaplot 14.0 software (Systat Software Inc. Palo Alto, California, United States) with the Kaplan–Meier estimator and the *F*-test. The statistics of the aggregation assay were performed with the Sigmaplot software using the ANOVA statistical test with a confidence interval of 95%. Meanwhile, for the chemotaxis index, the *F*-test was used.

Conclusions

Four piano-stool complexes containing Ru(II) (**1**), Os(II) (**2**), Ir(III) (**3**) and Rh(III) (**4**) were prepared from the same ligand **L1**. All the structurally related organometallic compounds were stable in PBS solution and the crystal structure of the Rh(III) compound confirmed the typical "three-legged piano-stool" geometry for this type of metal complexes.

Investigation of the effect of **1–4** on the aggregation of Aβ40 *in vitro* suggested that all of them favour an alternative folding pathway, impeding the formation of mature fibres. However, the metal centre seems to play a crucial role in their inhibiting activities. Group 8 metal complexes **1** and **2** led to analogous overall inhibition of amyloid aggregation (*ca.* 70%), but following distinct mechanisms of action: Ru(II) compound **1** delayed both the nucleation and the fibril elongation steps, while the Os(II) complex **2** acted by accelerating the nucleation process but slowing down the fibril elongation. Group 9 metal complexes **3** and **4** inhibited almost completely the aggregation of Aβ40, Rh(III) complex **4** being slightly stronger than Ir(III) compound **3**. Consequently, the aggregates formed with **3** and **4** were remarkably smaller than those formed with **1** and **2**. ESI-MS analysis revealed that Aβ40 displaces chloride and **L1** ligand to bind the metal centre of compounds **1**, **3** and **4**, but no evidence of such interaction was found for **2**.

In vivo studies revealed that **2** and **4** were able to significantly reduce the number of amyloid aggregates in the body muscle wall of *C. elegans* nematodes. It can be noted that **2** was more efficient than **4** *in vivo*, in contrast to the *in vitro* studies. For instance, treatment of the CL4176 strain of *C. elegans* with **2** delayed the paralysis onset by up to 7 hours while **4** did not rescue this paralysis phenotype. Remarkably, complex **2** also protected the nematode's neurons against Aβ-induced toxicity, as shown by the chemotaxis assays performed with the mutant strain CL2355. It can be stressed here that the activity differences observed between the *in vitro* and *in vivo* experiments should encourage carrying out both types of studies when investigating the activity of a potential drug.

To the best of our knowledge, **2** is the first reported osmium complex showing high efficacy in the inhibition of Aβ aggregation, both *in vitro* and *in vivo*. The promising data achieved with this organoosmium compound indicate that such metal complexes represent potential candidates for the development of potential anti-AD agents targeting Aβ.

Author contributions

Conceptualization: G. V., J. R., A. B. C., F. G.-H., P. G. Data curation: G. V., R. S., L. A. B., S. H.-G., P. B. Funding acquisition: J. R., F. G.-H., P. G. Investigation: G. V., R. S., L. A. B., A. B. C., S. H.-G., P. B. Methodology: G. V., R. S., L. A. B., A. B. C., S. H.-G. Project administration: G. V., J. R., A. B. C., F. G.-H., P. G. Resources: J. R., A. B. C., F. G.-H., P. G. Software: G. V., R. S., L. A. B., S. H.-G. Supervision: J. R., A. B. C., F. G.-H., P. G. Validation: G. V., J. R., A. B. C., F. G.-H., P. G. Writing – original draft: G. V., A. B. C. Writing – review & editing: G. V., J. R., A. B. C., S. H.-G., F. G.-H., P. G.

Data availability

Crystallographic data for complex **4** has been deposited at CCDC 2359733. For ESI and crystallographic data in CIF or other electronic format see **https://doi.org/10.1039/d4qi01460j**.

Conflicts of interest

There are no conflicts to declare.

Acknowledgements

Financial support from the Spanish Ministerio de Ciencia e Innovación-Agencia Estatal de Investigación (Projects PID2020-115537RB-I00, PCI2021-122027-2B, PID2021-122850NB-I0, PID2021-127863OB-I00 and PID2021-122896NB-I00; MCIU/AEI/10.13039/501100011033) and from European Union NextGenerationEU/PRTR is kindly acknowledged. P. G. thanks the Catalan Institution for Research and Advanced Studies (ICREA).

References

1 D. S. Knopman, H. Amieva, R. C. Petersen, G. Chetelat, D. M. Holtzman, B. T. Hyman, R. A. Nixon and D. T. Jones, Alzheimer disease, *Nat. Rev. Dis. Primers*, 2021, **7**, 21.

2 M. P. Murphy and H. LeVine, Alzheimer's Disease and the Amyloid-beta Peptide, *J. Alzheimer's Dis.*, 2010, **19**, 311–323.
3 P. V. Fish, D. Steadman, E. D. Bayle and P. Whiting, New approaches for the treatment of Alzheimer's disease, *Bioorg. Med. Chem. Lett.*, 2019, **29**, 125–133.
4 J. L. Cummings, T. Morstorf and K. Zhong, Alzheimer's disease drug-development pipeline: few candidates, frequent failures, *Alzheimers Res. Ther.*, 2014, **6**, 7.
5 Y. L. Yi and M. H. Lim, Current understanding of metal-dependent amyloid-beta aggregation and toxicity, *RSC Chem. Biol.*, 2023, **4**, 121–131.
6 X. H. Wang, X. Y. Wang and Z. J. Guo, Metal-involved theranostics: An emerging strategy for fighting Alzheimer's disease, *Coord. Chem. Rev.*, 2018, **362**, 72–84.
7 L. Grcic, G. Leech, K. Kwan and T. Storr, Targeting misfolding and aggregation of the amyloid-beta peptide and mutant p53 protein using multifunctional molecules, *Chem. Commun.*, 2024, **60**, 1372–1388.
8 A. Rauk, The chemistry of Alzheimer's disease, *Chem. Soc. Rev.*, 2009, **38**, 2698–2715.
9 D. J. Selkoe, The molecular pathology of alzheimers-disease, *Neuron*, 1991, **6**, 487–498.
10 A. I. Bush and R. E. Tanzi, Therapeutics for Alzheimer's disease based on the Metal Hypothesis, *Neurotherapeutics*, 2008, **5**, 421–432.
11 N. Puentes-Diaz, D. Chaparro, D. Morales-Morales, A. Flores-Gaspar and J. Ali-Torres, Role of Metal Cations of Copper, Iron, and Aluminum and Multifunctional Ligands in Alzheimer's Disease: Experimental and Computational Insights, *ACS Omega*, 2023, **8**(5), 4508–4526.
12 P. Faller and C. Hureau, Bioinorganic chemistry of copper and zinc ions coordinated to amyloid-beta peptide, *Dalton Trans.*, 2009, 1080–1094, DOI: **10.1039/b813398k**.
13 C. Haass and D. Selkoe, If amyloid drives Alzheimer disease, why have anti-amyloid therapies not yet slowed cognitive decline?, *PLoS Biol.*, 2022, **20**, 15.
14 A. Pasieka, D. Panek, N. Szalaj, A. Espargaro, A. Wieckowska, B. Malawska, R. Sabate and M. Bajda, Dual Inhibitors of Amyloid-beta and Tau Aggregation with Amyloid-beta Disaggregating Properties: Extended In Cellulo, In Silico, and Kinetic Studies of Multifunctional Anti-Alzheimer's Agents, *ACS Chem. Neurosci.*, 2021, **12**, 2057–2068.
15 X. Shao, C. R. Yan, C. Wang, C. L. Wang, Y. Cao, Y. Zhou, P. Guan, X. L. Hu, W. L. Zhu and S. C. Ding, Advanced nanomaterials for modulating Alzheimer's related amyloid aggregation, *Nanoscale Adv.*, 2022, **5**, 46–80.
16 K. D. Fasae, A. O. Abolaji, T. R. Faloye, A. Y. Odunsi, B. O. Oyetayo, J. I. Enya, J. A. Rotimi, R. O. Akinyemi, A. J. Whitworth and M. Aschner, Metallobiology and therapeutic chelation of biometals (copper, zinc and iron) in Alzheimer's disease: Limitations, and current and future perspectives, *J. Trace Elem. Med. Biol.*, 2021, **67**, 21.
17 S. Ben-Shushan and Y. Miller, Neuropeptides: roles and activities as metal chelators in neurodegenerative diseases, *J. Phys. Chem. B*, 2021, **125**, 2796–2811.
18 G. Veurink, G. Perry and S. K. Singh, Role of antioxidants and a nutrient rich diet in Alzheimer's disease, *Open Biol.*, 2020, **10**, 200084.
19 M. Simunkova, S. H. Alwasel, I. M. Alhazza, K. Jomova, V. Kollar, M. Rusko and M. Valko, Management of oxidative stress and other pathologies in Alzheimer's disease, *Arch. Toxicol.*, 2019, **93**, 2491–2513.
20 S. Laurent, M. R. Ejtehadi, M. Rezaei, P. G. Kehoe and M. Mahmoudi, Interdisciplinary challenges and promising theranostic effects of nanoscience in Alzheimer's disease, *RSC Adv.*, 2012, **2**, 5008–5033.
21 Y. Lian, Y. J. Jia, J. Wong, X. F. Zhou, W. Song, J. Guo, C. L. Masters and Y. J. Wang, Clarity on the blazing trail: clearing the way for amyloid-removing therapies for Alzheimer's disease, *Mol. Psychiatry*, 2024, **29**, 297–305.
22 E. Drummond and T. Wisniewski, Alzheimer's disease: experimental models and reality, *Acta Neuropathol.*, 2017, **133**, 155–175.
23 J. M. Suh, G. Kim, J. Kang and M. H. Lim, Strategies Employing Transition Metal Complexes To Modulate Amyloid-beta Aggregation, *Inorg. Chem.*, 2019, **58**, 8–17.
24 D. J. Hayne, S. Lim and P. S. Donnelly, Metal complexes designed to bind to amyloid-beta for the diagnosis and treatment of Alzheimer's disease, *Chem. Soc. Rev.*, 2014, **43**, 6701–6715.
25 T. Storr, Multifunctional compounds for the treatment of Alzheimer's disease, *Can. J. Chem.*, 2021, **99**, 1–9.
26 L. M. F. Gomes, J. C. Bataglioli and T. Storr, Metal complexes that bind to the amyloid-beta peptide of relevance to Alzheimer's disease, *Coord. Chem. Rev.*, 2020, **412**, 15.
27 H. Liu, Y. W. Qu and X. H. Wang, Amyloid beta-targeted metal complexes for potential applications in Alzheimer's disease, *Future Med. Chem.*, 2018, **10**, 679–701.
28 K. H. Chen and M. C. Cui, Recent progress in the development of metal complexes as beta-amyloid imaging probes in the brain, *MedChemComm*, 2017, **8**, 1393–1407.
29 B. Jiang and A. A. Marti, Probing Amyloid Nanostructures using Photoluminescent Metal Complexes, *Eur. J. Inorg. Chem.*, 2021, **2021**, 4408–4424.
30 G. Bort, S. Catoen, H. Borderies, A. Kebsi, S. Ballet, G. Louin, M. Port and C. Ferroud, Gadolinium-based contrast agents targeted to amyloid aggregates for the early diagnosis of Alzheimer's disease by MRI, *Eur. J. Med. Chem.*, 2014, **87**, 843–861.
31 T. G. Chan, C. L. Ruehl, S. V. Morse, M. Simon, V. Rakers, H. Watts, F. A. Aprile, J. J. Choi and R. Vilar, Modulation of amyloid-beta aggregation by metal complexes with a dual binding mode and their delivery across the blood-brain barrier using focused ultrasound, *Chem. Sci.*, 2021, **12**, 9485–9493.
32 L. He, X. S. Wang, D. S. Zhu, C. Zhao and W. H. Du, Methionine oxidation of amyloid peptides by peroxovanadium complexes: inhibition of fibril formation through a distinct mechanism, *Metallomics*, 2015, **7**, 1562–1572.
33 D. E. S. Silva, M. P. Cali, W. M. Pazin, E. Carlos-Lima, M. T. S. Trevisan, T. Venancio, M. Arcisio-Miranda, A. S. Ito

and R. M. Carlos, Luminescent Ru(II) Phenanthroline Complexes as a Probe for Real-Time Imaging of A beta Self-Aggregation and Therapeutic Applications in Alzheimer's Disease, *J. Med. Chem.*, 2016, **59**, 9215–9227.

34 E. Babu, P. M. Mareeswaran, V. Sathish, S. Singaravadivel and S. Rajagopal, Sensing and inhibition of amyloid-beta based on the simple luminescent aptamer-ruthenium complex system, *Talanta*, 2015, **134**, 348–353.

35 B. Y. W. Man, H. M. Chan, C. H. Leung, D. S. H. Chan, L. P. Bai, Z. H. Jiang, H. W. Li and D. L. Ma, Group 9 metal-based inhibitors of beta-amyloid (1-40) fibrillation as potential therapeutic agents for Alzheimer's disease, *Chem. Sci.*, 2011, **2**, 917–921.

36 A. F. Martins, A. C. Oliveira, J. F. Morfin, D. V. Laurents, E. Toth and C. Geraldes, Associating a negatively charged GdDOTA-derivative to the Pittsburgh compound B for targeting A beta amyloid aggregates, *J. Biol. Inorg. Chem.*, 2016, **21**, 83–99.

37 N. A. Vyas, S. S. Bhat, A. S. Kumbhar, U. B. Sonawane, V. Jani, R. R. Joshi, S. N. Ramteke, P. P. Kulkarni and B. Joshi, Ruthenium(II) polypyridyl complex as inhibitor of acetylcholinesterase and A beta aggregation, *Eur. J. Med. Chem.*, 2014, **75**, 375–381.

38 N. A. Vyas, S. N. Ramteke, A. S. Kumbhar, P. P. Kulkarni, V. Jani, U. B. Sonawane, R. R. Joshi, B. Joshi and A. Erxleben, Ruthenium(II) polypyridyl complexes with hydrophobic ancillary ligand as A beta aggregation inhibitors, *Eur. J. Med. Chem.*, 2016, **121**, 793–802.

39 L. Messori, M. Camarri, T. Ferraro, C. Gabbiani and D. Franceschini, Promising in Vitro anti-Alzheimer Properties for a Ruthenium(III) Complex, *ACS Med. Chem. Lett.*, 2013, **4**, 329–332.

40 X. S. Wang, D. S. Zhu, C. Zhao, L. He and W. H. Du, Inhibitory effects of NAMI-A-like ruthenium complexes on prion neuropeptide fibril formation, *Metallomics*, 2015, **7**, 837–846.

41 M. P. Cali, L. M. B. Pereira, M. D. Teodoro, T. A. Sellani, E. G. Rodrigues and R. M. Carlos, Comparison of A beta (1-40, 1-28, 11-22, and 29-40) aggregation processes and inhibition of toxic species generated in early stages of aggregation by a water-soluble ruthenium complex, *J. Inorg. Biochem.*, 2021, **215**, 6.

42 J. C. Bataglioli, L. M. F. Gomes, C. Maunoir, J. R. Smith, H. D. Cole, J. McCain, T. Sainuddin, C. G. Cameron, S. A. McFarland and T. Storr, Modification of amyloid-beta peptide aggregation via photoactivation of strained Ru(ii) polypyridyl complexes, *Chem. Sci.*, 2021, **12**, 7510–7520.

43 S. E. Huffman, G. K. Yawson, S. S. Fisher, P. J. Bothwell, D. C. Platt, M. A. Jones, C. G. Hamaker and M. I. Webb, Ruthenium(III) complexes containing thiazole-based ligands that modulate amyloid-beta aggregation, *Metallomics*, 2020, **12**, 491–503.

44 G. K. Yawson, M. F. Will, S. E. Huffman, E. T. Strandquist, P. J. Bothwell, E. B. Oliver, C. F. Apuzzo, D. C. Platt, C. S. Weitzel, M. A. Jones, G. M. Ferrence, C. G. Hamaker and M. I. Webb, A Dual-Pronged Approach: A Ruthenium(III) Complex That Modulates Amyloid-beta Aggregation and Disrupts Its Formed Aggregates, *Inorg. Chem.*, 2022, **61**, 2733–2744.

45 B. J. Wall, M. F. Will, G. K. Yawson, P. J. Bothwell, D. C. Platt, C. F. Apuzzo, M. A. Jones, G. M. Ferrence and M. I. Webb, Importance of Hydrogen Bonding: Structure-Activity Relationships of Ruthenium(III) Complexes with Pyridine-Based Ligands for Alzheimer's Disease Therapy, *J. Med. Chem.*, 2021, **64**, 10124–10138.

46 J. Kang, J. S. Nam, H. J. Lee, G. Nam, H. W. Rhee, T. H. Kwon and M. H. Lim, Chemical strategies to modify amyloidogenic peptides using iridium(III) complexes: coordination and photo-induced oxidation, *Chem. Sci.*, 2019, **10**, 6855–6862.

47 D. L. Ma, D. S. H. Chan and C. H. Leung, Group 9 Organometallic Compounds for Therapeutic and Bioanalytical Applications, *Acc. Chem. Res.*, 2014, **47**, 3614–3631.

48 G. S. Yellol, J. G. Yellol, V. B. Kenche, X. M. Liu, K. J. Barnham, A. Donaire, C. Janiak and J. Ruiz, Synthesis of 2-pyridyl-benzimidazole iridium(III), ruthenium(II), and platinum(II) complexes. study of the activity as inhibitors of amyloid-beta aggregation and neurotoxicity evaluation, *Inorg. Chem.*, 2015, **54**, 470–475.

49 H. O. Gulcan, A. Mavideniz, M. F. Sahin and I. E. Orhan, Benzimidazole-derived Compounds Designed for Different Targets of Alzheimer's Disease, *Curr. Med. Chem.*, 2019, **26**, 3260–3278.

50 S. Ali, M. Asad, S. Maity, W. Zada, A. A. Rizvanov, J. Iqbal, B. Babak and I. Hussain, Fluoro-benzimidazole derivatives to cure Alzheimer's disease: In-silico studies, synthesis, structure-activity relationship and in vivo evaluation for beta secretase enzyme inhibition, *Bioorg. Chem.*, 2019, **88**, 102936.

51 J. Yellol, S. A. Perez, G. Yellol, J. Zajac, A. Donaire, G. Vigueras, V. Novohradsky, C. Janiak, V. Brabec and J. Ruiz, Highly potent extranuclear-targeted luminescent iridium(III) antitumor agents containing benzimidazole-based ligands with a handle for functionalization, *Chem. Commun.*, 2016, **52**, 14165–14168.

52 M. A. Bennett and A. K. Smith, Arene ruthenium(II) complexes formed by dehydrogenation of cyclohexadienes with ruthenium(III) trichloride, *J. Chem. Soc., Dalton Trans.*, 1974, 233–241, DOI: 10.1039/dt9740000233.

53 W. A. Kiel, R. G. Ball and W. A. G. Graham, Carbonyl-eta-hexamethylbenzene complexes of osmium - carbon-hydrogen activation by (eta-C6Me6)Os(CO)(H)2, *J. Organomet. Chem.*, 1990, **383**, 481–496.

54 C. White, A. Yates and P. M. Maitlis, in *Transition Metal Organometallics and Ligands*, ed. R. N. Grimes, Inorganic Syntheses, Inc., 1992, ch. 53, vol. 29, pp. 228–234.

55 Y. Kashiwame, M. Watanabe, K. Araki, S. Kuwata and T. Ikariya, Synthesis, Structure, and Proton-Transfer Reactions of Bronsted Acidic Pyridylpyrazole Complexes of Ruthenium, *Bull. Chem. Soc. Jpn.*, 2011, **84**, 251–258.

56 Q. F. Zhang, R. D. Adams and W. H. Leung, Syntheses, spectroscopic properties and crystal structures of two orga-

noruthenium(II) complexes of bipyridines: {Cp*Ru(2,2′-bipy)}(2)(mu-Cl) PF6 and {(eta(6)-p-cymene)Ru}(2)(mu-OH)(2)(4,4′-bipy) (2) BF4 (4), *Inorg. Chim. Acta*, 2006, **359**, 978–983.

57 H. Naiki, K. Higuchi, M. Hosokawa and T. Takeda, Fluorometric-determination of amyloid fibrils invitro using the fluorescent dye, thioflavine-T, *Anal. Biochem.*, 1989, **177**, 244–249.

58 R. Sabaté, M. Gallardo and J. Estelrich, An autocatalytic reaction as a model for the kinetics of the aggregation of β-amyloid, *Biopolymers*, 2003, **71**, 190–195.

59 M. Iljina, G. A. Garcia, A. J. Dear, J. Flint, P. Narayan, T. C. T. Michaels, C. M. Dobson, D. Frenkel, T. P. J. Knowles and D. Klenerman, Quantitative analysis of co-oligomer formation by amyloid-beta peptide isoforms, *Sci. Rep.*, 2016, **6**, 28658.

60 C. D. Link, Expression of human beta-amyloid peptide in transgenic Caenorhabditis elegans, *Proc. Natl. Acad. Sci. U. S. A.*, 1995, **92**, 9368–9372.

61 J. Drake, C. D. Link and D. A. Butterfield, Oxidative stress precedes fibrillar deposition of Alzheimer's disease amyloid β-peptide (1-42) in a transgenic *Caenorhabditis elegans* model, *Neurobiol. Aging*, 2003, **24**, 415–420.

62 L. Diomede, S. Rigacci, M. Romeo, M. Stefani and M. Salmona, Oleuropein Aglycone Protects Transgenic C. elegans Strains Expressing Aβ42 by Reducing Plaque Load and Motor Deficit, *PLoS One*, 2013, 8, e58893.

63 C. D. Link, V. Fonte, C. M. Roberts, B. Hiester, M. A. Silverman and G. H. Stein, The β amyloid peptide can act as a modular aggregation domain, *Neurobiol. Dis.*, 2008, **32**, 420–425.

64 A. Gea-González, S. Hernández-García, P. Henarejos-Escudero, P. Martínez-Rodríguez, F. García-Carmona and F. Gandía-Herrero, Polyphenols from traditional Chinese medicine and Mediterranean diet are effective against Aβ toxicity *in vitro* and *in vivo* in *Caenorhabditis elegans*, *Food Funct.*, 2022, **13**, 1206–1217.

65 L. E. Dosanjh, M. K. Brown, G. Rao, C. D. Link and Y. Luo, Behavioral Phenotyping of a Transgenic *Caenorhabditis elegans* Expressing Neuronal Amyloid-β, *J. Alzheimer's Dis.*, 2010, **19**, 681–690.

66 A. Gioran, Y. Paikopoulos, E. Panagiotidou, A. E. I. Rizou, G. I. Nasi, V. D. Dimaki, K. D. Vraila, D. S. Bezantakou, P. M. Spatharas, N. C. Papandreou, V. Magafa, F. N. Lamari, V. A. Iconomidou and N. Chondrogianni, Beneficial Effects of Sideritis clandestina Extracts and Sideridiol against Amyloid β Toxicity, *Antioxidants*, 2024, **13**, 261.

67 G. M. Sheldrick, *SAINT and SADABS*, 2012.

68 G. M. Sheldrick, SHELXT - integrated space-group and crystal-structure determination, *Acta Crystallogr., Sect. A: Found. Adv.*, 2015, **71**, 3–8.

69 G. M. Sheldrick, Crystal structure refinement with SHELXL, *Acta Crystallogr., Sect. C: Struct. Chem.*, 2015, **71**, 3–8.

70 A. Espargaró, A. Medina, O. Di Pietro, D. Muñoz-Torrero and R. Sabate, Ultra rapid in vivo screening for anti-Alzheimer anti-amyloid drugs, *Sci. Rep.*, 2016, **6**, 23349.

71 N. Stroustrup, B. E. Ulmschneider, Z. M. Nash, I. F. López-Moyado, J. Apfeld and W. Fontana, The *Caenorhabditis elegans* Lifespan Machine, *Nat. Methods*, 2013, **10**, 665–670.

72 M. A. Guerrero-Rubio, S. Hernández-García, F. García-Carmona and F. Gandía-Herrero, Extension of life-span using a RNAi model and *in vivo* antioxidant effect of *Opuntia* fruit extracts and pure betalains in *Caenorhabditis elegans*, *Food Chem.*, 2019, **274**, 840–847.

73 O. Margie, C. Palmer and I. Chin-Sang, *C. elegans* Chemotaxis Assay, *J. Visualized Exp.*, 2013, e50069, DOI: **10.3791/50069**.

